Progress in Additive Manufacturing
https://doi.org/10.1007/s40964-026-01670-3

RESEARCH

Extending artificial-intelligence-assisted single bead geometry prediction to multi-bead interaction in fused granulate fabrication

Daniele Vanerio[1,2] · Mario Guagliano[1] · Sara Bagherifard[1]

Received: 14 January 2026 / Accepted: 23 March 2026

Abstract

Accurate prediction of the cross-sectional geometry of deposited beads is essential for improving process control in Fused Granulate Fabrication (FGF), a key process within the Large Format Additive Manufacturing (LFAM) family. Building upon the previous model for single bed shape prediction, this work addresses the complex problem of reconstructing the full cross-sectional shape of polymer beads in multi-bead configurations, focusing on both adjacent and superimposed beads, through an Artificial Neural Network (ANN). A structured dataset was generated by varying critical process parameters, namely layer height, screw speed, and bead center distance. The ANN, designed with two hidden layers and supported by image processing techniques, successfully captured the geometric features of the deposited material, reaching a mean absolute error of 10.22% across all tested conditions. Unlike traditional methods that approximate only a limited number of contour points, the approach proposed here, enables full-profile prediction, offering a deeper understanding of bead interactions and the dynamics of layer formation. The findings represent a significant step forward aimed at improving the geometric accuracy and the process control in LFAM applications, contributing to a better understanding of the role of the key process parameters.

Keywords Large format additive manufacturing · Machine learning · Artificial neural network · Fused granulate fabrication · Bead shape prediction

Abbreviations

AM	Additive manufacturing
AMAPE	Adapted mean absolute percentage error
ANN	Artificial neural network
BW	Black and white
CNC	Computer numerical control
CNN	Convolutional neural network
CS	Cold spray
CSAM	Cold spray additive manufacturing
DED	Directed energy deposition
FDM	Fused deposition modelling
FGF	Fused granulate fabrication
LFAM	Large format additive manufacturing
LKOCV	Leave k out cross validation
MAE	Mean absolute error
MAPE	Mean absolute percentage error
MXAE	Maximum absolute error
MXAPE	Maximum absolute percentage error
ML	Machine learning
MSE	Mean squared error
IoU	Intersection over union
PCA	Principal components analysis
PP-GF	Glass-fibre reinforced polypropylene
R^2	Coefficient of determination
RGB	Red, green and blue
SLM	Selective laser melting
WAAM	Wire arc additive manufacturing

✉ Sara Bagherifard
sara.bagherifard@polimi.it

Daniele Vanerio
daniele.vanerio@polimi.it

Mario Guagliano
mario.guagliano@polimi.it

[1] Politecnico di Milano, Milan, Italy

[2] Caracol AM Srl, Milan, Italy

Published online: 15 April 2026

1 Introduction

Fused Granulate Fabrication (FGF) is a material extrusion process within Large Format Additive Manufacturing (LFAM) that uses pellet feedstock to melt thermoplastics or fiber-reinforced thermoplastics. The technology, which typically relies on screw extruders, offers advantages such as lower costs, higher throughput, and improved mechanical properties compared to filament-based methods. FGF's high deposition rates and cost-effective feedstock are making it increasingly popular in industries like aerospace, naval, and automotive [1–3]. These parts offer benefits like simplified assembly, improved structural integrity, and reduced material waste. FGF is often complemented by CNC milling to achieve the precision and surface finish required for applications such as mold production, where these factors directly impact the final component's functions. This technology's readiness for large format applications has been highlighted in a recent review paper [4].

Many of the challenges in FGF are related to low resolution and geometric inaccuracies [1], particularly in predicting how individual beads, the fundamental building blocks of a printed part, interact. One of the most critical issues is the formation of defects due to suboptimal spacing between adjacent beads (Fig. 1). When the bead spacing is too small, excess material accumulates, negatively impacting the deposition of subsequent layers and potentially resulting in increasing geometric deviations as the build height increases. Conversely, excessive spacing leads to the formation of inter-bead or inter-track voids, which compromise part integrity. This issue was previously observed in Fused Deposition Modeling (FDM) by Duty et al. [5], and a recent study by Lim et al. [6] reported a similar phenomenon in FGF. In their work, voids took the shape of a diamond-like star, also referred to as "astroids". Through experimental design and regression analysis, the previous studies focused on identifying optimal process parameters, such as screw speed, layer height, and overlap percentage, to minimize void formation [6]. The staircase effect is another relevant aspect to consider. It refers to the characteristic stepped pattern observed on the lateral surfaces of components produced through additive manufacturing (AM) processes [7]. Owing to the larger feature sizes involved, this phenomenon is even more pronounced in LFAM processes [4], where increased bead width and bead height lead to a coarser external surface finish. In this context, an accurate prediction of bead geometry becomes essential to enable the prediction of this geometric defect in the final component.

Each layer is affected by those beneath it, thus, modelling the interactions between new and existing layers is crucial. Previous studies on single bead geometry prediction in FGF and FDM have encountered several critical limitations:

- Geometric models, such as those by Aksoy et al. [8] and Ahn et al. [9], rely on simplified assumptions (e.g., elliptical bead shapes) and limited parameters, which lead to low accuracy in predictions.
- Numerical models like those by Balta et al. [10] and Comminal et al. [11, 12] and Serdeczny et al. [13, 14] are computationally expensive and exhibit relatively low accuracy, with predictions often affected by systematic errors.
- Machine Learning (ML) has demonstrated strong potential in predicting bead geometry for various AM and LFAM technologies like Selective Laser Melting (SLM), Directed Energy Deposition (DED), and Wire Arc Additive Manufacturing (WAAM) [15–20]. However, these models are typically limited to predicting basic bead parameters such as height and width, rather than providing a comprehensive prediction of the entire shape. Some studies have applied Artificial Neural Networks (ANNs) to predict bead contours for technologies like Cold Spray Additive Manufacturing (CSAM) [21–23] and DED [24], but these models struggle with more complex geometries, such as undercuts or overlapping beads. While the model by Ikeuchi et al. [21] is precise for CSAM, its variable resolution limits its ability

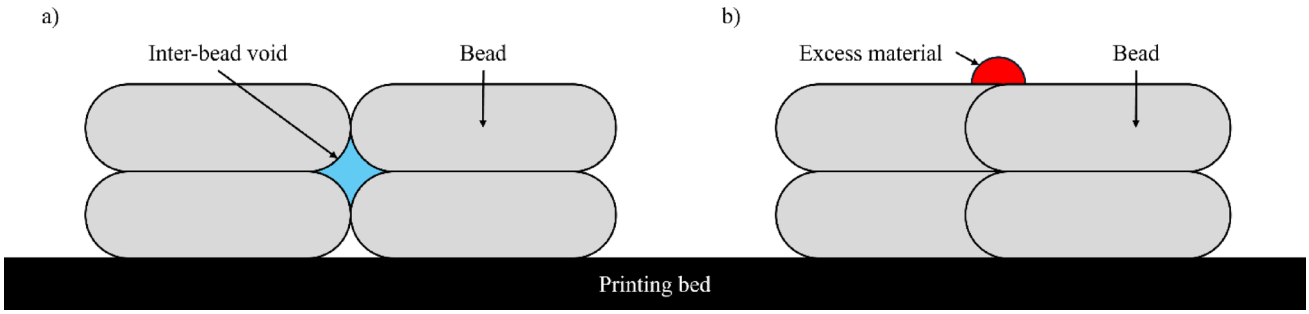

Fig. 1 Geometric challenges in bead deposition. **a** Inter-bead voids formed due to excessive center distance between adjacent beads. **b** Excess material accumulation caused by insufficient center distance, negatively impacting the deposition of subsequent layers and leading to cumulative geometric inaccuracies during part growth

to predict elongated beads or more complex shapes in multi-bead or multi-layer configurations.

Wang et al. [25] conducted a prediction of multiple-bead geometric parameters for Laser-Arc Hybrid Additive Manufacturing; however, their approach is limited to adjacent beads and only predicts height and flatness. Similarly, Asadi et al. [26] performed predictions of only height and waviness for superimposed multiple-bead deposits. An attempt to predict the geometry of multiple beads was made by Ikeuchi et al. [27] and Falco at al. [28], whose model, although effective for Cold Spray Additive Manufacturing (CSAM), relies on deposit growth models specific to CSAM and not extendable to other LFAM technologies. On the other hand, the only simulation developed for FGF by Pibulchinda et al. [29] models the interaction between multiple beads. Although they showed that process parameters significantly influence the bead-to-bead contact area, the results of their simulations on adjacent multiple beads were not compared with experimental data, leaving the validity of their predictions unconfirmed.

Rizzieri et al. [30] proposed a neural network model for 3D concrete printing that uses Fourier descriptors to predict the full cross-sectional contour of single and overlapping beads. The method can capture complex features such as necking at the inter-layer contact and is computationally efficient.

However, the analysis is limited to single beads and superimposed beads (Fig. 2c), while adjacent bead (Fig. 2b) deposition is not addressed. In addition, the selection criteria for the experimental cases from the literature used to test the method are not clearly discussed. Finally, the performance indicators adopted, namely height, width and area, and the contact length in the case of superimposed beads, are not sufficient for a comprehensive assessment of geometric prediction accuracy, as they only describe global parameters and do not quantify how accurately complex local features of the contour are captured.

In a previous work [31], it was demonstrated the use of an ANN model to predict the geometry of FGF's single beads, based on images, with constant resolution and high accuracy. Building up on this previous study, through ANN modeling and experimental validation, here we demonstrate for the first time a comprehensive prediction of multiple FGF beads, including both adjacent and superimposed configurations, capturing complex inter-bead interactions and highlighting the versatility of our approach. Additionally, with numerical parameters as input and a binary image as output, our model has the potential to be adapted to other LFAM and AM technologies and extended to predict internal features of the beads. The results on multiple beads confirm the effectiveness of our model, showing its ability to adapt to the most relevant process parameters.

2 Methods

2.1 Research questions

To investigate the factors influencing the geometry of FGF beads, three distinct configurations were analyzed: single beads, adjacent beads, and superimposed beads. Key process parameters, including layer height, extruder screw speed, and inter-bead distance, were systematically varied to study their effect on bead shape. A central objective of this work was to determine whether limited datasets are sufficient to train an ANN model capable of accurately predicting bead geometry, including multiple-bead configurations where complex inter-bead interactions occur, such as local material accumulation or variations in deposition caused by the presence of previously deposited beads. The study also evaluated whether the predictive accuracy achieved for multiple beads is comparable to that obtained for single beads, providing insight into the model's applicability across different deposition strategies. Finally, the relative contribution of image pre-processing and post-processing steps to the overall prediction error was assessed, in order to quantify how much of the observed discrepancies are attributable to these data handling procedures versus the ANN predictions themselves.

2.2 Process parameter levels and dataset strategy

To investigate the behavior of adjacent and superimposed beads, three distinct sets of experiments were conducted. The initial set examined individual beads, serving as a reference for centering the cross-sections of multiple beads; the second set investigated adjacent beads, and the third set analyzed superimposed beads. The definitions of multiple bead configurations are illustrated schematically in Fig. 2. In all experiments and simulations, both adjacent and superimposed bead configurations consist of two beads. In these experiments, key process parameters were varied, including layer height, extruder screw speed, and the distance between the centers of the beads. Both layer height and bead center distance are depicted in Fig. 2. These experimental settings are consistent with those used by Pibulchinda et al. [29], who varied parameters such as layer height, bed velocity to extrudate velocity ratio (which is influenced by screw speed), and bead overlap percentage (which is analogous to the distance between the centers of the beads in our study).

While it is straightforward to set equally spaced constant levels for the other process parameters, this is not feasible

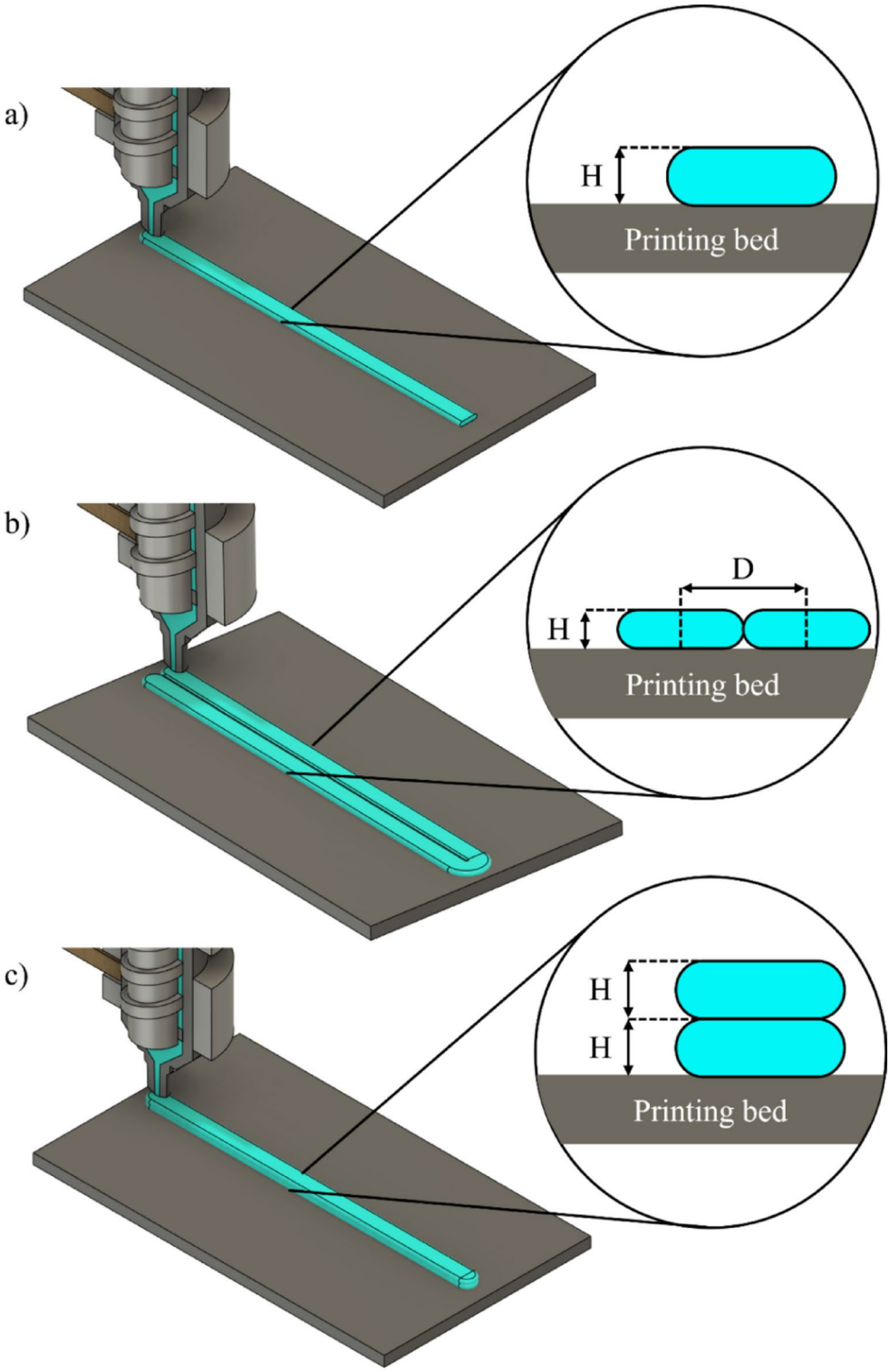

Fig. 2 Schematic representation of bead configurations and printing strategy used in the experiments. The enlarged view areas in **a**, **b**, and **c** represent cross-sections of the deposited beads. **a** Single bead. **b** Adjacent beads. **c** Superimposed beads

for the center-to-center distance of adjacent beads. When varying the layer height (H) and screw speed (S) while keeping this distance constant, some combinations would result in beads too far apart to make contact, whereas others would produce excessive overlap, leading to irregular bead shapes. Therefore, boundary values were defined based on a series of considerations. These are solely intended to establish limits for the dataset and do not influence the prediction procedure.

First, the cross-sectional area A is assumed to be proportional to the screw speed S, since the screw speed directly determines the volumetric material flow rate and the robot

Table 1 Input variables' levels in the case of single beads

Level	Layer height (mm)	Screw speed (rpm)
1	1.5	12
2	2.0	14
3	2.5	16

Table 2 Input variables' levels for the training of the ANN in the case of adjacent beads

Level	Layer height (mm)	Screw speed (rpm)	k ratio (mm^2/rpm)
1	1.5	12	1.000
2	2.0	14	1.225
3	2.5	16	1.450

speed is kept constant (Eq. 1), as also observed in other studies [32].

$$A \propto S \tag{1}$$

Subsequently, by embedding the bead in a rectangular bounding box, for a constant cross-sectional area A, the width w and layer height H are inversely proportional (Eq. 2).

$$A \propto \frac{w}{H} \tag{2}$$

Finally, to maintain comparable conditions across different levels of layer height and screw speed, we impose that the center-to-center distance D between adjacent beads is proportional to their width w (Eq. 3).

$$D \propto w \tag{3}$$

From these considerations, Eq. 4 is derived. Here, a constant $k$is introduced, with three levels determined experimentally. The minimum k value corresponds to beads placed so close that any further reduction in center-to-center distance would lead to process instability, while the maximum value ensures the minimum overlap required to avoid gaps between adjacent beads.

$$D = k\frac{S}{H} \tag{4}$$

This formulation provides meaningful boundary values for the dataset and defines the levels for the process parameters.

To ensure a sufficiently broad and well-distributed training dataset, three levels were selected for each input process variable. The first and third levels correspond to the empirically tested minimum and maximum operational limits of the machine, beyond which sample production was unsuccessful, for instance beads that did not adhere to the build plate or samples exhibiting highly irregular cross-sections along their length. The second level corresponds to the intermediate value between the minimum and maximum limits. As reported in Tables 1 and 2, and 3, and in the supplementary materials (Tables S1–S3), the operational limits are 1.5 mm and 2.5 mm for layer height, 12 rpm and 16 rpm for screw speed, and 1.000 to 1.450 for the k ratio. This selection ensures that the training data spans the full feasible range of the process while including only valid samples. The considered variables are H and S for all configurations, namely single, superimposed, and adjacent beads. For the adjacent bead configuration, the additional parameter k was also included. This results in 9 parameter combinations for single beads, 9 combinations for superimposed beads, and 27 combinations for adjacent beads. The selected parameter levels are reported in Tables 1 and 2, and 3, respectively, while all parameter combinations are listed in Tables S1–S3 in the Supplementary Materials.

Table 3 Input variables' levels for the training of the ANN in the case of superimposed beads

Level	Layer height (mm)	Screw speed (rpm)
1	1.5	12
2	2.0	14
3	2.5	16

The rationale for including nine randomized single bead samples is that, for a given layer height and screw speed, the first bead in both adjacent and superimposed configurations corresponds exactly to a single bead. Therefore, single beads serve as a direct geometrical reference for evaluating the interaction effects occurring in multi-bead configurations. In adjacent beads, the second bead modifies the geometry of the first through lateral interaction, while in superimposed beads, the upper bead is deposited on top of a first bead that is geometrically equivalent to a single bead. This approach ensures consistent baseline conditions across configurations and facilitates a clearer visual interpretation of bead-to-bead interaction effects.

Consequently, the final dataset consists of 18 single bead samples (9 full-factorial and 9 randomized), 36 adjacent bead samples (27 full-factorial and 9 randomized), and 12 superimposed bead samples (9 full-factorial and 3 randomized).

An ideal data split of 75% for training, 10% for validation, and 15% for testing was assumed. Due to the different sample sizes associated with each bead configuration, different strategies were adopted for the partitioning of training, validation, and testing datasets.

- For the single bead configuration, an adjustment to maintain the intended split ratio was applied. Specifically, five randomized combinations (ID14 to ID18) were

reassigned to the training set in order to approximate the 75-10-15 proportion.

- For the adjacent-bead configuration, the larger number of combinations and their distribution among full-factorial and randomized datasets, allowed straightforward adherence to the ideal split. In this case, all randomized samples were allocated to the validation and testing sets according to the predefined proportions.
- In the case of superimposed beads, the dataset was particularly limited. To ensure reliable performance evaluation while retaining sufficient data for training, a custom Leave-*K*-Out Cross-Validation (LKOCV) scheme was employed. The fixed combinations were consistently retained in the training set, while the randomized samples were alternately assigned to validation and testing, as detailed in Tables S6–S8 of the Supplementary Materials. In each iteration, two samples were used for validation and one for testing, while the remaining data were used for training. This procedure was repeated until each sample from the three randomized sets had been assigned to both validation and testing roles at least once. Although this approach does not correspond to classical leave-one-out cross-validation, it retains its core principle of maximizing data usage while minimizing estimation bias. Variants of leave-*k*-out cross-validation have been applied in manufacturing and process modelling tasks when dealing with small datasets, as they provide more stable and representative error estimates [33, 34].

The resulting cross-sections are presented in Figures S1–S4 for the training datasets and in Figures S5–S7 for the validation and testing datasets, respectively.

Among the nine randomized input combinations generated for single bead deposition, three (IDs 14, 17, and 18) coincided with conditions already included in the training set. Therefore, they were not physically reproduced but are still reported for completeness. In contrast, samples corresponding to IDs 29 and 30 could not be fabricated due to the excessive center-to-center distance between beads, which caused them to remain completely separated. As a result, their production was unsuccessful.

Although in some applications, such as process simulation or fault diagnosis, ANNs have proven capable of both interpolation and extrapolation with high accuracy [35–37], interpolative predictions generally yield more reliable results. For this reason, our analysis was limited to the interpolation domain, as reported in previous studies using a similar approach [22, 31]. Having defined three levels for each variable and established the operating bounds, the intermediate level was placed at the midpoint of the range to ensure a balanced exploration of the input space. Hence, extrapolation beyond the trained range would correspond to process conditions leading to failed deposition, making such extrapolation irrelevant. In addition, it is reasonable to expect that prediction performance gradually deteriorates as inputs approach the operational boundaries, since these regions increasingly tend toward extrapolation rather than interpolation. All other parameters, aside from those explicitly mentioned, were kept constant throughout the experiments.

To ensure consistent positioning of the sample images within the frame, all Red-Green-Blue (RGB) images were first converted to Black and White (BW). Then, the single bead samples with parameters matching those of the adjacent and superimposed configurations were centered by aligning their centroid to the center of the frame, followed by a symmetry-based adjustment.

2.3 Materials and experimental setup

All samples were fabricated using a robotic FGF system developed by Caracol AM (Barlassina, Italy), specifically the Heron AM™ 300 platform equipped with a high-flow extruder featuring an 8 mm diameter nozzle. The extrusion head was mounted on a KUKA KR120 R3100 Quantec-2 robotic arm (KUKA, Augsburg, Germany). The feedstock was a 30% short glass fiber-reinforced homopolymer polypropylene, dried at 80 °C for 2 h prior to processing, following material specifications. Extrusion was performed under steady-state thermal conditions, with barrel temperatures set to 240 °C, 245 °C, and 250 °C from zone 1 to zone 3. Printing operations began only once thermal stabilization was reached. Toolpaths were generated using Caracol Builder (Caracol AM), a proprietary slicing software. For each toolpath point, the nozzle-substrate distance was manually calibrated based on direct measurements. Deposition followed linear toolpaths with sampling points spaced at 100 mm intervals, for a total bead length of 500 mm. The robot operated at a transverse speed of 50 mm/s for all depositions. Cross-sectional analysis was consistently performed at the same location along the path to ensure comparability across all samples. According to ISO 9283, the robot's positional repeatability is ±0.05 mm.

After printing, all samples were sectioned using a cut-off machine Tecmet 2000 (Milan, Italy), model C301K. Each specimen was cut to the same length of 40 mm to ensure consistency in subsequent analyses.

Cross-sectional imaging was then performed using a Zeiss SteREO Discovery.V12 optical microscope (Zeiss, Oberkochen, Germany) equipped with a Zeiss Axiocam 305 color camera and operated via the Zeiss ZEN Microscopy Software. Since the sample cross-sections exceeded the field of view of the microscope, the "Panorama Interactive" function of the software was employed. This feature allows

the user to manually acquire multiple adjacent image tiles across the sample area using a manual stage and then stitch them into a single high-resolution composite image [38]. The resulting stitched images were used for all subsequent analysis.

2.4 Design and training of the artificial neural network

All the image processing, training, and testing operations were carried out using MATLAB® R2025a. The ANN architecture employed in this study was a multilayer perceptron with two hidden layers (5 and 10 neurons, respectively). Other models, such as traditional regression and Random Forest, have been outperformed by ANNs in analogous studies, even for simpler cases considering only bead width and height [39]. Convolutional Neural Networks (CNNs) are advantageous when the input consists of structured data, such as images or grids. They have been applied, for example, to defect detection, geometric deviation control [40], and even bead geometry prediction. However, in the latter case, structured inputs have been used, i.e., molten pool data acquired from pyrometers or cameras [41]. In our case, the input consists solely of discrete process parameters, so the spatial feature extraction offered by CNNs is unnecessary.

Images were scaled down in size to reduce the computational effort while preserving the geometric characteristics needed for shape prediction. For single and superimposed beads, the image resolution was reduced to 64×64 pixels, while for adjacent beads, a slightly larger size of 128×128 pixels was maintained, since the original images were wider due to the use of the "interactive panorama" function in the Zeiss ZEN software during acquisition. In all cases, Principal Component Analysis (PCA) was applied after image pre-processing to further reduce dimensionality, improve training performance, and retain the most relevant geometric features. This method has proven to be effective in similar applications and allows image matrices to be compressed while preserving spatial information.

After PCA, all data were normalized between -1 and 1 to stabilize and accelerate the training. The ANN was trained using the Bayesian regularization backpropagation algorithm, well-suited for small datasets and for mitigating overfitting. For the hidden and output layers, the hyperbolic tangent sigmoid activation function was employed. The performance function was again set to Mean Squared Error (MSE).

A validation set was employed only for early stopping. It was observed that 10 training epochs led to good performance across the more limited datasets used here (particularly in the case of superimposed and single beads), and with the more complex feature involved in the case of adjacent beads.

Finally, the ANN outputs were converted back into cross-sectional profiles using inverse PCA, and a thresholding step was applied to re-sharpen contours. The images were then upscaled and smoothed using 2D Gaussian filtering, producing final predictions at original resolution.

A summary of the overall workflow, from pre-processing to prediction, is presented in Fig. 3.

3 Results

3.1 Performance indicators definition

To ensure a comprehensive and robust assessment of the model performance, a wide set of evaluation metrics was employed. These performance indicators were selected to provide complementary insights into prediction accuracy, and match those already used in previous works for consistency and comparability. All metrics reflect standard definitions, except for AMAPE, which differs slightly from the traditional MAPE and has been previously used in literature for analogous performance evaluations. For clarity, the following acronyms are reported. When a metric deviates from standard definitions, the corresponding formula is also provided in the text.

- MAE (Mean Absolute Error).
- MXAE (Maximum Absolute Error).
- AMAPE (Adjusted Mean Absolute Percent Error).

$$AMAPE = \frac{A_{mis} + A_{exc}}{A_s} * 100 = 100 \frac{1}{A_s} \sum_m \sum_n |A_{mn} - B_{mn}| \tag{5}$$

- MXAPE (Maximum Absolute Percent Error).
- R^2 (Coefficient of Determination).

$$R = \frac{\sum_m \sum_n \left(A_{mn} - \bar{A}\right)\left(B_{mn} - \bar{B}\right)}{\sqrt{\left(\sum_m \sum_n \left(A_{mn} - \bar{A}\right)^2\right)\left(\sum_m \sum_n \left(B_{mn} - \bar{B}\right)^2\right)}} \tag{6}$$

In Eqs. 5 and 6, A is the predicted image and B is the experimental one; A_{mn} is the value of A in the pixel of coordinates (m, n) and B_{mn} is the value of B in the pixel of coordinates (m, n). In Eq. 5 A_{mis} represents the area of the predicted bead that is missing with respect to the experimental cross-section, while A_{exc} denotes the area of the predicted bead that does not overlap with the experimental cross-section. A_s is the total area of the experimental cross-section. In Eq. 6 $\bar{A}$ is the mean value of the predicted image and $\bar{B}$ is the mean value of the experimental cross-section image.

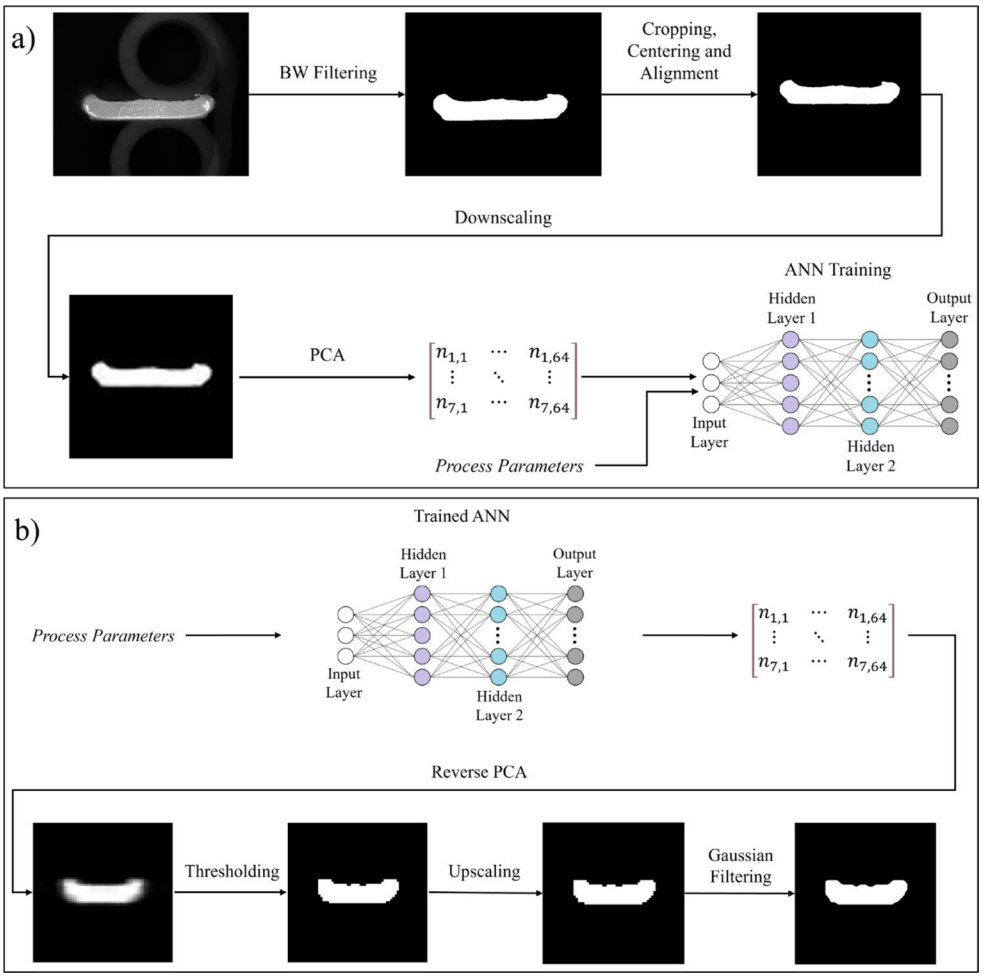

Fig. 3 Process workflow. **a** Image pre-processing and training of the ANN. Main phases: binary filtering, cropping, centering, alignment, downscaling, PCA and ANN training. **b** ANN prediction. Main phases: ANN prediction, inverse PCA, thresholding, upscaling and Gaussian filtering [31]

Notably, AMAPE and the Intersection over Union (IoU) are closely related metrics. In fact, they would be complementary if not for the additional term in the IoU denominator corresponding to false positive material (A_{exc}) predicted by the simulation. In this work, AMAPE is retained for continuity with previous studies, while IoU is also reported because it is widely used in machine learning for bounding box regression [42] and in image segmentation [43]. This correspondence further reinforces the validity and robustness of AMAPE as a metric, as it aligns with a standard measure for evaluating the quality of pixel-wise or geometric predictions. Including both metrics provides a more comprehensive quantitative assessment of prediction accuracy and facilitates comparison with existing literature. The IoU is formally defined in Eq. 7.

$$IoU = \frac{A \cap B}{A \cup B} = \frac{A_s - A_{mis}}{A_s + A_{exc}} \tag{7}$$

3.2 Network structure

The network architecture used in this study is illustrated in Fig. 4. Although the general structure is built upon previous works [31], maintaining the same number of layers and neurons, some adjustments were made in the input parameters to consider the peculiar aspects of the present study. Specifically, for the single and superimposed beads, the network receives only two input parameters: layer height and screw speed. In contrast, for adjacent beads, the network incorporates an additional parameter, i.e. the center distance between beads.

3.3 Model performance evaluation

Figures 5, 6 and 7 present the visual comparison between predicted and experimental cross-sections for the testing samples, shown at their original resolution. Specifically, Fig. 5 shows results for single beads, included for general assessment purposes, while Figs. 6 and 7 report results for superimposed and adjacent beads, respectively. In these visualizations, white regions indicate overlapping areas

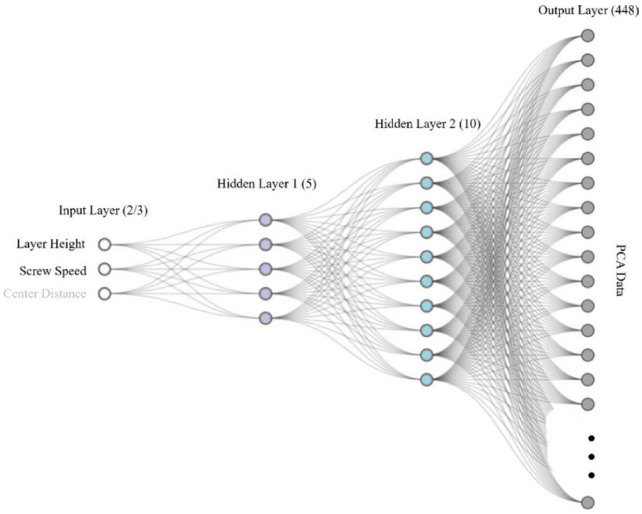

Fig. 4 Structure of the developed ANN

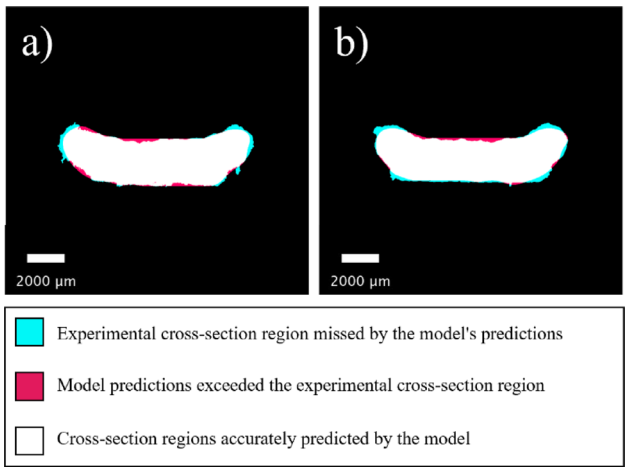

Fig. 5 Comparison of single beads experimental cross-sections and images generated by the ANN for test samples. **a** Sample ID 12. **b** Sample ID 13. Input parameters for each sample are reported in Table 6. Regions of accurate prediction are indicated in white while discrepancies are indicated in cyan and red

between prediction and experiment (i.e., accurate prediction), cyan regions correspond to areas missed by the model, and red regions highlight material falsely predicted by the network.

These comparisons clearly show a strong agreement between predictions and experimental results. Beyond the performance indicators, the major geometric features, such as bead height, bead width, and more specific characteristics of the general shape, including the curvature of single beads, the size change between the first and second bead in the superimposed configurations, and the presence and position of small material accumulations where adjacent beads touch, can all be observed in Figs. 5, 6 and 7.

The main discrepancies occur in regions with sharp or irregular geometries. Notably, the cyan and red areas are small relative to the overall bead size, which indicates that the predictions are generally accurate. In Fig. 5, corresponding to single beads, the highest accuracy is observed. Here, errors are mostly distributed along the bead edges, and the most noticeable difference is that the simulated beads appear smoother and lack some of the sharper features present in the experimental images.

For superimposed beads (Fig. 6), the overall shape is well captured, but the prediction of the upper bead is less precise. Deviations are primarily found at the contact region between the two beads, the central top region, and the left and right ends of the upper bead.

Adjacent beads exhibit the largest errors due to the more complex physics involved. Unlike superimposed beads, where material is deposited on top of a previous layer, here the molten material interacts laterally with the already deposited bead, causing irregular geometries and slight upward protrusions. The model correctly identifies the location of this accumulation, but the predicted bump is significantly smoothed compared to the experimental bead and does not fully reproduce its actual shape. Prediction errors are also visible at the left and right extremities of the bead.

Table 6 Detailed ANN prediction results for all test samples, including input parameters, sample IDs, and performance indicators for single, superimposed, and adjacent bead configurations

Sample ID	Layer height (mm)	Screw speed (rpm)	k ratio (mm^2/rpm)	Center distance (mm)	MAE (mm^2)	AMAPE (%)	R^2	IoU
Single beads								
12	2.3	13	–	–	14.721	8.305	0.950	0.912
13	2.2	13	–	–	16.593	9.362	0.943	0.909
Superimposed beads								
64-a	1.9	16	–	–	13.465	7.597	0.950	0.926
65-b	1.5	15	–	–	21.509	12.135	0.920	0.887
66-c	2.3	13	–	–	17.937	10.112	0.935	0.903
Adjacent beads								
50	2	12	1.010	6.06	24.352	13.739	0.917	0.872
51	1.6	14	1.020	8.93	22.493	12.690	0.923	0.880
52	1.9	14	1.100	8.11	16.288	9.189	0.946	0.911
53	2	12	1.140	6.84	26.142	14.749	0.909	0.863
54	2	14	1.080	7.56	16.022	9.039	0.947	0.912

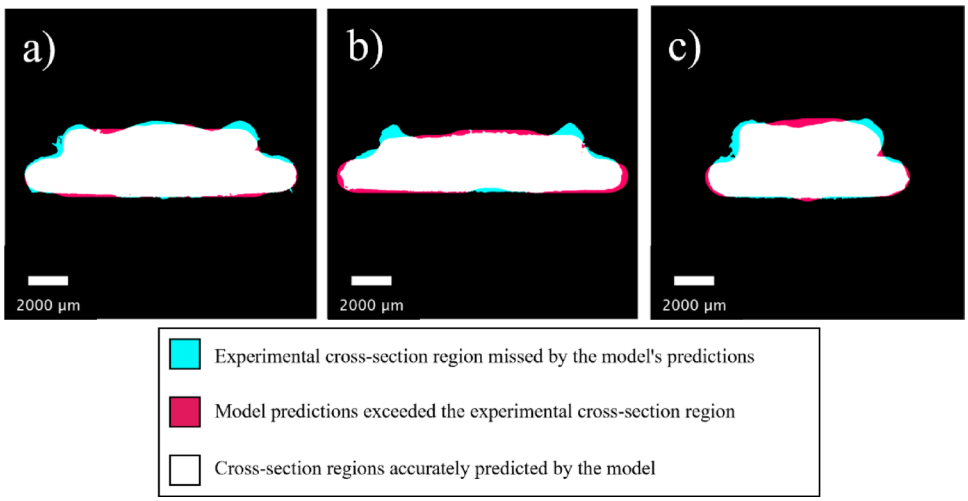

Fig. 6 Comparison of superimposed beads experimental cross-sections and images generated by the ANN for test samples. **a** Sample ID 64. **b** Sample ID 65. **c** Sample ID 66. Input parameters for each sample are reported in Table 6. Regions of accurate prediction are indicated in white while discrepancies are indicated in cyan and red

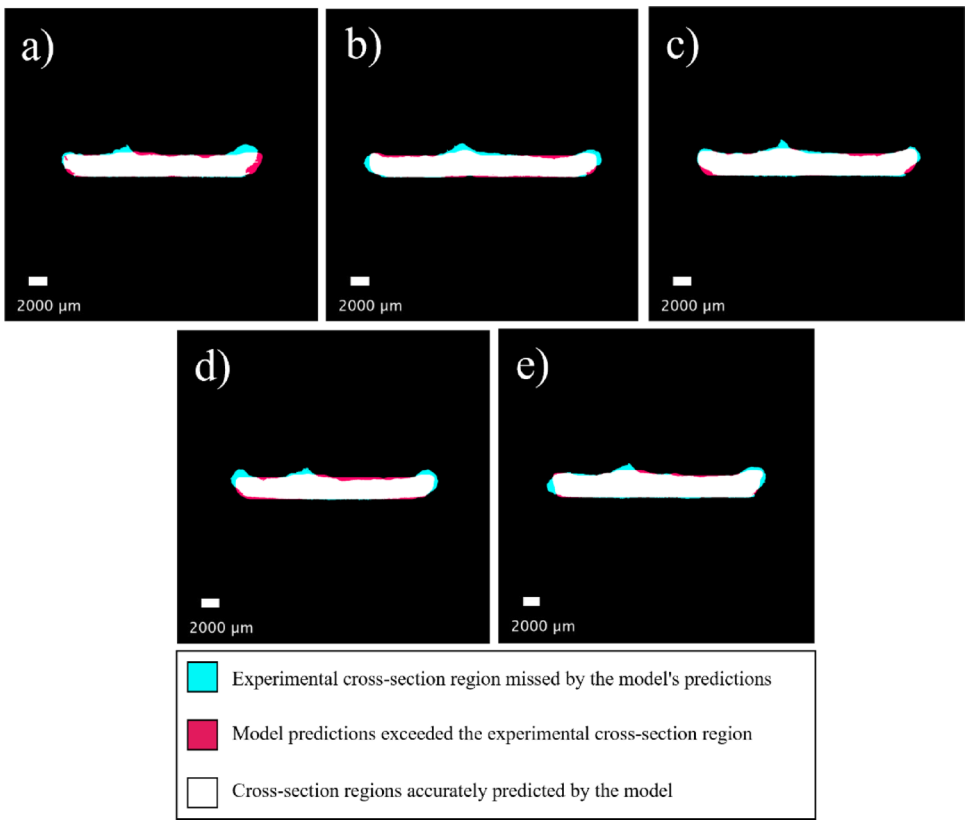

Fig. 7 Comparison of adjacent beads experimental cross-sections and images generated by the ANN for test samples. **a** Sample ID 50. **b** Sample ID 51. **c** Sample ID 52. **d** Sample ID 53. **e** Sample ID 54. Input parameters for each sample are reported in Table 6. Regions of accurate prediction are indicated in white while discrepancies are indicated in cyan and red

The sources of these errors can be traced to several aspects. The initial image downscaling, while necessary, leads to a loss of detail, and the same applies to the PCA compression stage. Although inverse PCA, upscaling, and Gaussian filtering are applied afterward, some information is inevitably lost during the earlier steps, which are essential to reduce computational effort. This results in predicted bead shapes that are significantly smoother than the experimental ones and causes local features, such as sharp edges or small bumps, to appear less pronounced.

Additionally, minor process instabilities and the limited positioning accuracy of the robot may introduce asymmetries. For single beads, high repeatability is sufficient, but in multi-bead configurations, such as superimposed and adjacent beads, the second bead is deposited in a different position due to variations in layer height and center distance. This, combined with the more complex physical interactions involved, results in slightly lower accuracy compared to single bead predictions.

Even when accounting for these factors, the ANN has intrinsic limitations. While it can capture complex patterns

Table 4 Comparison of AMAPE contributions from pre-processing/post-processing and ANN prediction

Configuration	Pipeline-only AMAPE (%)	Pipeline + NN AMAPE (%)	ANN increment (%)
Single	6.77	8.83	2.06
Superimposed	6.41	9.95	3.54
Adjacent	6.98	11.88	4.90

The table reports the average error introduced by image pre-processing and post-processing alone (downscaling, PCA/inverse PCA, upscaling, Gaussian filtering) and the additional error introduced by the ANN prediction for single, superimposed, and adjacent bead configurations

within the training data, it does not encode the underlying physics of the deposition process, and architectures such as the multilayer perceptron used here naturally tend to produce smooth outputs [44]. Consequently, local deviations with strong variations are difficult to predict, and the network cannot produce perfect results. This limitation also implies that extrapolation beyond the range of parameters used during training is expected to be less accurate, as the model can only interpolate within the space it has observed.

The quantitative performance of the model is summarized in Table 5 corresponds to the single, superimposed, and adjacent bead configurations. The results obtained for single beads serve primarily as a consistency check and confirm the validity of the dataset, yielding an AMAPE of 8.83%, which is remarkably close to the 8.88% reported in a previous work [31]. For the superimposed configuration, the average AMAPE under the LKOCV strategy is 9.95% ± 1.86%, computed over the three different splits, which yield values of 7.60%, 12.13%, and 10.12% for samples ID64, ID65, and ID66, respectively. For the adjacent configuration, the AMAPE value is 11.88%. Averaging across the three configurations, with equal weight given to each, results in an overall AMAPE of 10.22%. This confirms the general reliability of the framework across different deposition strategies. The MXAPE values are only 2–3% higher than their corresponding mean AMAPE, further supporting the robustness of the approach. Additionally, the R^2 values remain high across all cases, reaching approximately 0.93 for both superimposed and adjacent beads. It is worth noting that a substantial portion of the error originates from the pre-processing and post-processing steps applied to the images, i.e., downscaling, PCA, reverse PCA, upscaling, and Gaussian filtering. These steps contribute AMAPE values of 6.77%, 6.41%, and 6.98%, for the single, superimposed, and adjacent bead configurations, respectively. These values were obtained by applying the full pre-processing pipeline to the raw images and then performing the post-processing to restore them to the original format, without performing the ANN-based prediction. The additional error introduced on average by the ANN is 2.06%, 3.54%, and 4.90% for the single, superimposed, and adjacent configurations, respectively. These results indicate that the dominant contribution to the overall error originates from the pre-processing and post-processing steps rather than the ANN itself. However, separating the two contributions makes it clear that the ANN error becomes proportionally more significant for complex multi-bead configurations than for single beads. A summary of the results for each fold of the pre-processing-only evaluation, as well as the additional error introduced by the ANN for all configurations, is reported in Table 4.

Overall, the numerical results support the visual evidence, confirming that the proposed framework performs consistently well across different bead configurations. Extended performance data for each individual sample can be found in the Supplementary material (Table 5).

The results presented in this section demonstrate that the proposed framework is not only capable of accurately predicting the geometry of single beads, but also of modeling the formation of multiple beads, including both adjacent and superimposed configurations. This confirms that the ANN does not merely learn how a single bead forms but is also able to capture the interaction mechanisms between a newly deposited bead and a previously printed one, under varying process conditions.

Despite the limited size of the datasets, the consistency and accuracy of the predictions validate the effectiveness of the adopted approach. This robustness can be attributed both to the architecture of the ANN itself and to the data management strategies implemented like the LKOCV strategy.

4 Conclusion and outlook

LFAM processes have been experiencing rapid growth in recent years. As these technologies mature, process control and the ability to predict the final properties of the printed components, first and foremost their geometry, are becoming increasingly important. In this study, we build upon previous work by not only, confirming the feasibility of cross-section prediction in LFAM, but significantly expanding its scope. We demonstrate a novel data-efficient approach capable of generating entire FGF cross-sectional geometries

Table 5 Summary of ANN prediction performance indicators

	MAE (mm^2)	MXAE (mm^2)	AMAPE (%)	MXAPE (%)	R^2	IoU
Single	15.66	16.59	8.83	9.36	0.946	0.911
Superimposed	17.64	21.51	9.95	12.13	0.935	0.905
Adjacent	21.06	26.14	11.88	14.75	0.928	0.888

with homogeneous resolution and low error. Across all bead configurations: single, superimposed, and adjacent, the model achieved an average AMAPE of 10.22% and an average R^2 of 0.936, confirming strong predictive performance. Furthermore, we show that this framework can accurately simulate multiple beads across different deposition configurations. These multi-bead cases are inherently complex, both in terms of geometry and underlying physical interactions. For the superimposed configuration, it should be noted that the dataset was relatively limited, which may have affected prediction variability; further investigation with more extensive datasets would be necessary to fully confirm the robustness of the approach for this specific case. Nevertheless, except for a few highly localized inaccuracies, the model achieved excellent predictive performance, as confirmed by all relevant quantitative indicators. Overall, the results confirm the robustness and practical applicability of the proposed approach across different bead configurations.

This advancement is a key step toward establishing a generalizable prediction framework for LFAM. Expanding the dataset in terms of materials, nozzle sizes, and process conditions will further improve the generalization capability of the proposed framework and support its applicability across a broader range of scenarios. While the current study focuses on an 8 mm nozzle and interpolation within the corresponding process space, the high-level network architecture and training strategy are expected to remain applicable to smaller nozzle sizes, provided that the network is trained on datasets reflecting the finer geometrical features and higher magnification required.

Future work will focus on extending the method to other LFAM technologies for the prediction of bead geometry. It may also be worth investigating whether the prediction of internal bead features can be feasibly integrated within this framework. In addition, similar neural network architectures and training strategies could be applied to non-geometric material properties, where outputs are numerical rather than image based, excluding image processing steps when not required. Even at its current stage, integration of this framework into the production workflow can enable better geometric control, reduce internal and surface defects, and support hybrid processes by optimizing subtractive process parameters.

Supplementary Information The online version contains supplementary material available at https://doi.org/10.1007/s40964-026-01670-3.

Acknowledgements The authors express their gratitude to Dr. Ludovica Rovatti (Politecnico di Milano, Italy) for her support in preparing the samples. SB acknowledges funding from the European Research Council (ERC) under the European Union's Horizon 2021 research and innovation programme (ArcHIDep ERC-Co project, grant agreement no. 101044228). Views and opinions expressed are, however, those of the authors only and do not necessarily reflect those of the European Union or the European Research Council Executive Agency. Neither the European Union nor the granting authority can be held responsible for them.

Author contributions DV designed the methodology, performed the experiments, processed the samples, implemented the code, conducted the analysis, and drafted the manuscript. SB and MG provided guidance during the experimental phase, validated the analytical methods, and contributed to manuscript review and revisions. All authors critically reviewed and approved the final version of the manuscript.

Funding Open access funding provided by Politecnico di Milano within the CRUI-CARE Agreement.

Data availability All data produced or analysed in the present article are included in the main text and its supplementary information files "Supplementary material". Other relevant data are available upon request.

Code availability The scripts developed for data processing and model implementation can be obtained from the corresponding author upon request.

Declarations

Competing interests The authors declare no competing interests.

Use of AI-based language editing tools Portions of this manuscript were refined for grammar and clarity using an AI-based language editing tool (ChatGPT). The tool was used solely for linguistic editing and did not generate scientific content, analysis, or conclusions. All scientific content was written, reviewed, and verified by the authors.

References

1. Vicente CMS, Sardinha M, Reis L et al (2023) Large-format additive manufacturing of polymer extrusion-based deposition systems: review and applications. Progress Additive Manuf. https://doi.org/10.1007/s40964-023-00397-9
2. Pignatelli F, Percoco G (2022) An application- and market-oriented review on large format additive manufacturing, focusing on polymer pellet-based 3D printing. Progress Additive Manuf. https://doi.org/10.1007/s40964-022-00309-3
3. Moreno Nieto D, Molina SI (2020) Large-format fused deposition additive manufacturing: a review. Rapid Prototyp J 26:793–799. https://doi.org/10.1108/RPJ-05-2018-0126

4. Vanerio D, Guagliano M, Bagherifard S (2024) Emerging trends in large format additive manufacturing processes and hybrid techniques. Progress Additive Manuf. https://doi.org/10.1007/s40964-024-00771-1
5. Duty CE, Kunc V, Compton B et al (2017) Structure and mechanical behavior of Big Area Additive Manufacturing (BAAM) materials. Rapid Prototyp J 23:181–189. https://doi.org/10.1108/RPJ-12-2015-0183
6. Lim A, Dehgahi S, Mohiuddin A et al (2024) Effect of process parameters on the void fraction and tensile strength of polyvinyl alcohol produced by fused granulate fabrication. Int J Adv Manuf Technol 134:2233–2250. https://doi.org/10.1007/s00170-024-14158-7
7. Carolo CB, Cooper L, RE O (2022) A review on the influence of process variables on the surface roughness of Ti-6Al-4V by electron beam powder bed fusion. Addit Manuf. https://doi.org/10.1016/j.addma.2022.103103
8. Doruk Aksoy EC, Balta DM, Tilbury K, Barton A (2020) control-oriented model for bead cross-sectional geometryin fused deposition modeling. In: American Control Conference (ACC). Denver, CO, USA, pp 474–480. https://doi.org/10.23919/ACC45564.2020.9147769
9. Ahn D, Kweon JH, Kwon S et al (2009) Representation of surface roughness in fused deposition modeling. J Mater Process Technol 209:5593–5600. https://doi.org/10.1016/j.jmatprotec.2009.05.016
10. Balta EC, Altınkaynak A (2022) Numerical and experimental analysis of bead cross-sectional geometry in fused filament fabrication. Rapid Prototyp J 28:1882–1894. https://doi.org/10.1108/RPJ-09-2021-0255
11. Comminal R, Serdeczny MP, Pedersen DB, Spangenberg J (2018) Numerical modeling of the strand deposition flow in extrusion-based additive manufacturing. Addit Manuf 20:68–76. https://doi.org/10.1016/j.addma.2017.12.013
12. Comminal R, Serdeczny MP, Pedersen DB, Spangenberg J (2019) Motion planning and numerical simulation of material deposition at corners in extrusion additive manufacturing. Addit Manuf. https://doi.org/10.1016/j.addma.2019.06.005
13. Serdeczny MP, Comminal R, Pedersen DB, Spangenberg J (2019) Numerical simulations of the mesostructure formation in material extrusion additive manufacturing. Addit Manuf 28:419–429. https://doi.org/10.1016/j.addma.2019.05.024
14. Serdeczny MP, Comminal R, Pedersen DB, Spangenberg J (2018) Experimental validation of a numerical model for the strand shape in material extrusion additive manufacturing. Addit Manuf 24:145–153. https://doi.org/10.1016/j.addma.2018.09.022
15. Le-Hong T, Lin PC, Chen JZ et al (2023) Data-driven models for predictions of geometric characteristics of bead fabricated by selective laser melting. J Intell Manuf 34:1241–1257. https://doi.org/10.1007/s10845-021-01845-5
16. Mohajernia B, Mirazimzadeh SE, Pasha A, Urbanic RJ (2022) Machine learning approaches for predicting geometric and mechanical characteristics for single P420 laser beads clad onto an AISI 1018 substrate. Int J Adv Manuf Technol 118:3691–3710. https://doi.org/10.1007/s00170-021-08155-3
17. Oh WJ, Lee CM, Kim DH (2022) Prediction of deposition bead geometry in wire arc additive manufacturing using machine learning. J Mater Res Technol 20:4283–4296. https://doi.org/10.1016/j.jmrt.2022.08.154
18. Xiong J, Zhang G, Hu J, Wu L (2014) Bead geometry prediction for robotic GMAW-based rapid manufacturing through a neural network and a second-order regression analysis. J Intell Manuf 25:157–163. https://doi.org/10.1007/s10845-012-0682-1
19. Lee JA, Sagong MJ, Jung J et al (2023) Explainable machine learning for understanding and predicting geometry and defect types in Fe-Ni alloys fabricated by laser metal deposition additive manufacturing. J Mater Res Technol 22:413–423. https://doi.org/10.1016/j.jmrt.2022.11.137
20. Subadra SP, Mayer E, Wachtel P, Sheikhi S (2024) Feasibility study on machine learning methods for prediction of process-related parameters during WAAM process using SS-316L filler material. Weld World 68:3205–3214. https://doi.org/10.1007/s40194-024-01855-w
21. Ikeuchi D, Vargas-Uscategui A, Wu X, King PC (2021) Data-efficient neural network for track profile modelling in cold spray additive manufacturing. Appl Sci (Switzerland) 11:1–12. https://doi.org/10.3390/app11041654
22. Ikeuchi D, Vargas-Uscategui A, Wu X, King PC (2019) Neural network modelling of track profile in cold spray additive manufacturing. Materials. https://doi.org/10.3390/ma12172827
23. Liu M, Wu H, Yu Z et al (2021) Description and prediction of multi-layer profile in cold spray using artificial neural networks. J Therm Spray Technol 30:1453–1463. https://doi.org/10.1007/s11666-021-01212-z
24. Gihr M, Rashid A, Melkote SN (2024) Bead geometry prediction and optimization for corner structures in directed energy deposition using machine learning. Addit Manuf. https://doi.org/10.1016/j.addma.2024.104080
25. Wang J, Feng L, Xu J et al (2025) Optimal process parameter combinations search for desired deposited layer geometry in laser-arc hybrid additive manufacturing based on multi-pass overlapping deposited layer contour prediction model and improved NSGA-II algorithm. Opt Laser Technol. https://doi.org/10.1016/j.optlastec.2025.112700
26. Asadi R, Ylä-Autio A, Wiikinkoski OH, Ituarte IF (2025) Multimodal deep learning-based on and off-axis melt pool monitoring for layer height and surface metrology predictions in directed energy deposition. J Intell Manuf. https://doi.org/10.1007/s10845-025-02714-1
27. Ikeuchi D, Vargas-Uscategui A, Wu X, King PC (2024) Data-driven overlapping-track profile modeling in cold spray additive manufacturing. J Therm Spray Technol 33:530–539. https://doi.org/10.1007/s11666-024-01733-3
28. Falco R, Jalayer M, Bagherifard S (2025) Enhanced geometrical control in cold spray additive manufacturing through deep neural network predictive models. Virtual Phys Prototyp. https://doi.org/10.1080/17452759.2025.2472388
29. Pibulchinda P, Barocio E, Favaloro AJ, Pipes RB (2023) Influence of printing conditions on the extrudate shape and fiber orientation in extrusion deposition additive manufacturing. Compos B Eng. https://doi.org/10.1016/j.compositesb.2023.110793
30. Rizzieri G, Lanteri F, Ferrara L, Cremonesi M (2025) ShapeGen3DCP: a deep learning framework for layer shape prediction in 3D concrete printing. Comput Struct. https://doi.org/10.1016/j.compstruc.2026.108142
31. Vanerio D, Guagliano M, Bagherifard S (2025) Machine learning image-based analysis for bead geometry prediction in fused granulate fabrication for large format additive manufacturing. npj Adv Manuf 2:8. https://doi.org/10.1038/s44334-025-00018-z
32. Labus Zlatanovic D, Hildebrand J, Bergmann JP (2023) The study of screw extrusion-based additive manufacturing of eco-friendly aliphatic polyketone. J Mater Res Technol 25:4125–4138. https://doi.org/10.1016/j.jmrt.2023.06.223
33. Jafarian F, Amirabadi H, Sadri J (2013) Integration of finite element simulation and intelligent methods for evaluation of thermo-mechanical loads during hard turning process. Proc Inst Mech Eng B J Eng Manuf 227:235–248. https://doi.org/10.1177/0954405412466995
34. Formisano A, Conte S, Papa I (2022) Neural network predictions of the impact behaviour of GFRP laminates. J Braz Soc Mech Sci Eng. https://doi.org/10.1007/s40430-022-03554-3

35. Tize Mha P, Dhondapure P, Jahazi M et al (2023) Interpolation and extrapolation performance measurement of analytical and ANN-based flow laws for hot deformation behavior of medium carbon steel. Metals (Basel). https://doi.org/10.3390/met13030633
36. El-Sari B, Biegler M, Rethmeier M (2021) Investigation of the extrapolation capability of an artificial neural network algorithm in combination with process signals in resistance spot welding of advanced high-strength steels. Metals (Basel). https://doi.org/10.3390/met11111874
37. Chouhan A, Gangsar P, Porwal R, Mechefske CK (2021) Artificial neural network–based fault diagnosis for induction motors under similar, interpolated and extrapolated operating conditions. Noise Vib Worldw 52:323–333. https://doi.org/10.1177/09574565211030709
38. Zeiss C, Gmbh M (2020) Software manual ZEISS ZEN core v3.2 ZEISS ZEN core v3.2 original manual
39. So MS, Mahdi MM, Kim DB, Shin JH (2024) Prediction of metal additively manufactured bead geometry using deep neural network. Sensors. https://doi.org/10.3390/s24196250
40. Esoso AA, Ikumapayi OM, Jen TC, Akinlabi ET (2023) Exploring machine learning tools for enhancing additive manufacturing: a comparative study. Ingenierie des Systemes d'Information 28:535–544. https://doi.org/10.18280/isi.280301
41. Jamnikar ND, Liu S, Brice C, Zhang X (2022) In-process comprehensive prediction of bead geometry for laser wire-feed DED system using molten pool sensing data and multi-modality CNN. Int J Adv Manuf Technol 121:903–917. https://doi.org/10.1007/s00170-022-09248-3
42. Rezatofighi H, Tsoi N, Gwak J et al (2019) Generalized intersection over union: a metric and a loss for bounding box regression. https://doi.org/10.1109/CVPR.2019.00075
43. Bebis G, Boyle R, Parvin Darko Koracin B et al (2016) Advances in visual computing. Springer, Switzerland https://doi.org/10.1007/978-3-319-50835-1
44. Niu H, Deng J, Hou F et al (2026) SharpNet: enhancing MLPs to represent functions with controlled non-differentiability. https://doi.org/10.48550/arXiv.2601.19683